

# Laser Patterned Flexible 4T Perovskite-Cu(In,Ga)Se<sub>2</sub> Tandem Mini-module with Over 18% Efficiency

Radha K. Kothandaraman, Huagui Lai, Abdessalem Aribia, Shiro Nishiwaki, Severin Siegrist, Maximilian Krause, Yannick Zwirner, Galo Torres Sevilla, Kerem Artuk, Christian M. Wolff, Romain Carron, Ayodhya N. Tiwari, and Fan Fu\*

Perovskite-Cu(In,Ga)Se<sub>2</sub> (CIGS) thin-film tandem technology provides an exciting prospect to achieve low-cost high-efficiency photovoltaic devices by high throughput roll-to-roll processing on flexible substrates. However, no report on flexible perovskite-CIGS mini-modules has been published due to scribing-related challenges in realizing near-infrared (NIR)-transparent perovskite mini-modules on flexible substrates. Herein, an NIR-transparent flexible perovskite mini-module with an efficiency of 10.8% and an NIR-transparency of over 75% is reported. All-laser scribed interconnection approach is used to realize monolithic interconnection of mini-modules on thermally sensitive soft flexible substrate. An analytical method is utilized to optimize the mini-module layout and achieve a geometric fill factor of over 93%. Further, as a proof of concept, a flexible perovskite-CIGS tandem mini-module with an efficiency of 18.4% on an aperture area of 2.03 cm<sup>2</sup> is demonstrated. To conclude, pathways for improving the efficiency of flexible NIR-transparent perovskite mini-modules are discussed.

materials and possibility of low-temperature processing make them ideal candidate for top solar cell in tandem application.<sup>[4]</sup> Further, the thin-film nature of the perovskite absorber provides a promising pathway to realize high-efficiency lightweight flexible tandem solar cells in combination with well-established thin-film Cu(In,Ga)Se<sub>2</sub> (CIGS) solar cells as bottom cell. The top perovskite cell can be processed on CIGS front encapsulation foil,<sup>[5]</sup> and can directly be integrated into the existing CIGS module production line (Figure S1, Supporting Information) to enable low-cost high-throughput R2R production of flexible tandem modules. The numerous advantages of flexible tandems can be used in applications such as wearable electronics,<sup>[6]</sup> building and transport integrated photovoltaics (PV),<sup>[7]</sup> and portable and indoor applications.<sup>[8]</sup>

## 1. Introduction


Metal halide perovskites have gained tremendous research attention due to their excellent optoelectronic properties, ease of fabrication, and potential for low-cost manufacturing.<sup>[1,2]</sup> This fueled the rapid advancement in the development of perovskite solar cells to reach a power conversion efficiency (PCE) of over 25% on rigid glass substrate.<sup>[3]</sup> Wide- and tunable-bandgap property of the perovskite

Perovskite-CIGS tandem solar cells in mechanically stacked 4-terminal (4T) and monolithically grown 2-terminal (2T) architecture have been demonstrated on both rigid and flexible substrates.<sup>[4]</sup> Perovskite-CIGS tandem solar cells on glass substrates have reached efficiencies of 27.1%<sup>[9]</sup> and 24.2%<sup>[10]</sup> on the 4T and 2T tandem architecture, respectively. Similarly, efficiencies of 21.06%<sup>[11]</sup> and 13.2%<sup>[12]</sup> have been achieved in 4T and 2T configuration on flexible substrates. However, besides two reports on 4T perovskite-CIGS tandem mini-modules on rigid substrates,<sup>[13,14]</sup> most of the published reports (4T and 2T) are confined to lab-scale sized tandem solar cells (<1 cm<sup>2</sup>).<sup>[4]</sup> The challenges pertaining to realizing near-infrared (NIR)-transparent perovskite mini-modules have hindered the progress of perovskite-CIGS tandem solar modules.

The perovskite modules are realized through interconnecting smaller area solar strips (subcell) in series by sequence of laser or mechanical scribing/patterning steps.<sup>[15]</sup> In this way, the parasitic resistance losses in the transparent conductive substrate are reduced by avoiding long transport distances. In general, the width of the subcell is optimized to limit the resistive losses in the transparent electrode.<sup>[16]</sup> While, the scribed area used for monolithic interconnection is minimized to a narrow width as they do not contribute to any PV power generation. The ratio of the active area in the module to the total aperture area is defined as the geometric fill factor (GFF), and is used as a figure of merit for module design. In the case of NIR-transparent perovskite mini-module, the presence of two resistive transparent

R. K. Kothandaraman, H. Lai, A. Aribia, S. Nishiwaki, S. Siegrist, M. Krause, Y. Zwirner, G. T. Sevilla, R. Carron, A. N. Tiwari, F. Fu  
Laboratory for Thin Films and Photovoltaics  
Empa-Swiss Federal Laboratories for Materials Science and Technology  
8600 Dübendorf, Switzerland  
E-mail: fan.fu@empa.ch

K. Artuk, C. M. Wolff  
Institute of Electrical and Microengineering (IEM)  
Photovoltaics and Thin-Film Electronics Laboratory (PV-Lab)  
École Polytechnique Fédérale de Lausanne (EPFL)  
2000 Neuchâtel, Switzerland

 The ORCID identification number(s) for the author(s) of this article can be found under <https://doi.org/10.1002/solr.202200392>.

© 2022 The Authors. Solar RRL published by Wiley-VCH GmbH. This is an open access article under the terms of the Creative Commons Attribution-NonCommercial License, which permits use, distribution and reproduction in any medium, provided the original work is properly cited and is not used for commercial purposes.

DOI: 10.1002/solr.202200392

contacts necessitates to limit the width of each subcell and increase the number of subcells in series to reduce resistive losses.<sup>[16]</sup> The increase in the number of subcells contributes to a larger fraction of the interconnection area and reduces the GFF of the mini-module. It is important to have an optimized module layout design to achieve a proper trade-off between resistive and interconnection losses to minimize the total fraction of power loss.<sup>[14,17,18]</sup>

In the initial demonstration of rigid perovskite-CIGS 4T tandem mini-modules on glass substrate, Paetzold and co-workers<sup>[14]</sup> developed monolithically interconnected NIR-transparent perovskite mini-modules with seven subcells with an efficiency of 12% on an aperture area of 3.76 cm<sup>2</sup>. The width of the subcell was limited to 2.86 mm to account for the high sheet resistance of the front and rear electrodes. Their perovskite mini-module exhibited an average NIR-transparency of around 75% and yielded a 4T tandem efficiency of 17.8% in combination with a CIGS bottom mini-module. In a follow-up work, Jaysankar et al.<sup>[13]</sup> used a similar module design, but incorporated a triple-cation perovskite absorber with improved optoelectronic quality as the top mini-module. The higher efficiency of NIR-transparent perovskite mini-module (14.4%) improved the 4T tandem mini-module efficiency to 20.1% on an aperture area of 4 cm<sup>2</sup>. In both the cases, a combination of laser and mechanical scribing was adopted to realize monolithic interconnection, and the mini-module displayed a GFF of 91%. Although these reports demonstrate the potential to realize NIR-transparent perovskite mini-module, the module layout design can be improved to achieve a higher GFF.

Until now, there are no published reports on NIR-transparent perovskite mini-module on flexible substrate. It is challenging to realize monolithic interconnection on flexible substrate. The soft nature of the flexible substrate restricts the use of mechanical scribing, and patterning using mask is not desirable as it would contribute to a higher dead-area losses.<sup>[5]</sup> An ideal approach for minimal dead-area loss is laser patterning. However, the laser pulse used for scribing induces thermal stress on the flexible polymer substrate and could cause physical damage. It is challenging to realize selective removal of layers without damaging the flexible substrate.

We have overcome the challenges of laser patterning on flexible substrates to realize an all-laser scribed monolithically interconnected NIR-transparent perovskite mini-modules on polymer film. We utilized an analytical method for designing optimum module layout to minimize resistive and interconnection losses in the mini-module. Then, we optimized the laser patterning process for selective removal of layers without causing any damage to the flexible substrate. Here, we report the development of flexible NIR-transparent perovskite mini-module of 10.8% efficiency, with an average NIR-transparency of 75% and a GFF of over 93%. In combination with a flexible CIGS mini-module, we demonstrate a proof-of-concept flexible 4T tandem mini-module with an efficiency of 18.4% on an aperture area of around 2 cm<sup>2</sup>. Finally, we discuss the origin of performance losses in the perovskite mini-module, and outline strategies for further development.

## 2. Results and Discussion

**Figure 1** shows the processing sequence followed for development of NIR-transparent perovskite mini-module on flexible substrates in a p–i–n device architecture. For the ease of sample

handling, the flexible polyethylene naphthalene (PEN) substrate is mounted to a glass substrate by gluing it with an adhesive epoxy. To reduce the parasitic absorption losses due to free carrier absorption in the transparent electrode, a high carrier mobility hydrogenated indium oxide (IO:H) layer is used as front electrode.<sup>[19]</sup> Compared to the commercial indium tin oxide (ITO)-coated PEN substrate, the IO:H-coated PEN substrate shows reduced absorption in the NIR region. (Figure S2, Supporting Information)

After the IO:H deposition, P1 scribing is carried out to isolate the TCO electrode into individual subcells. Next, poly(triarylamine) (PTAA) hole transport layer is deposited by spin coating. For conformal and pin-hole free coating of the perovskite layer, we utilized a hybrid deposition process with a combination of thermal evaporation and spin coating.<sup>[20]</sup> First, the inorganic halide template consisting of cesium iodide (CsI) and lead iodide (PbI<sub>2</sub>) is sequentially evaporated using thermal evaporation, and then, an organo-halide precursor solution comprising a mixture of formamidinium iodide (FAI) and formamidinium bromide (FABr) in ethanol is spin-coated on top of the inorganic halide template. The stack is annealed at 150 °C in an ambient atmosphere for 30 min to facilitate perovskite formation. Thermally evaporated C60 is used as the electron transport layer (ETL) to conformally cover the perovskite absorber. To protect the underlying layers from ion damage during TCO sputtering, SnO<sub>2</sub> buffer layer on top of the C<sub>60</sub> is grown by atomic layer deposition (ALD). Prior to the rear TCO deposition, P2 scribing is carried out to create a pathway to interconnect the adjacent subcells. After the sputtering of the indium zinc oxide (IZO) electrode, P3 scribing is performed to isolate the rear electrode between the subcells. The thermal budget of the whole processing sequence is limited to not more than 150 °C for processing compatibility on the flexible substrate. Detailed description of the mini-module fabrication is provided in the experimental section.

Active and dead areas in the mini-module are shown in Figure 1. The active area represents the strip of the subcell which contributes to PV power generation, and the dead area represents the strip of the subcell used for monolithic interconnection. An optimum width of the active area is required to minimize the resistive losses due to the presence of two transparent electrodes, and the interconnection width needs to be narrow to minimize the dead area losses.<sup>[18,21,22]</sup>

### 2.1. Design Consideration for NIR-Transparent Perovskite Mini-module

To evaluate the fraction of resistive and dead area losses in a NIR-transparent perovskite mini-module, an analytical method is used.<sup>[23,24]</sup> The fraction of resistive losses in the front and rear transparent electrodes is calculated using Equation (1) and (2), where  $R_{SH}$  denotes the sheet resistance of the TCO layer,  $J_{MPP}$  and  $V_{MPP}$  are the current density and voltage at the maximum power point (MPP) in small area cells, and  $W_A$ ,  $W_D$  are the width of active and dead areas, respectively. The resistive loss can be minimized by adopting a narrow  $W_A$ . However, this would lead to a higher fraction of dead area power loss as shown by Equation (3). A careful balance between resistive and dead area loss fractions is the key to minimize the total relative power loss (Equation (4)).

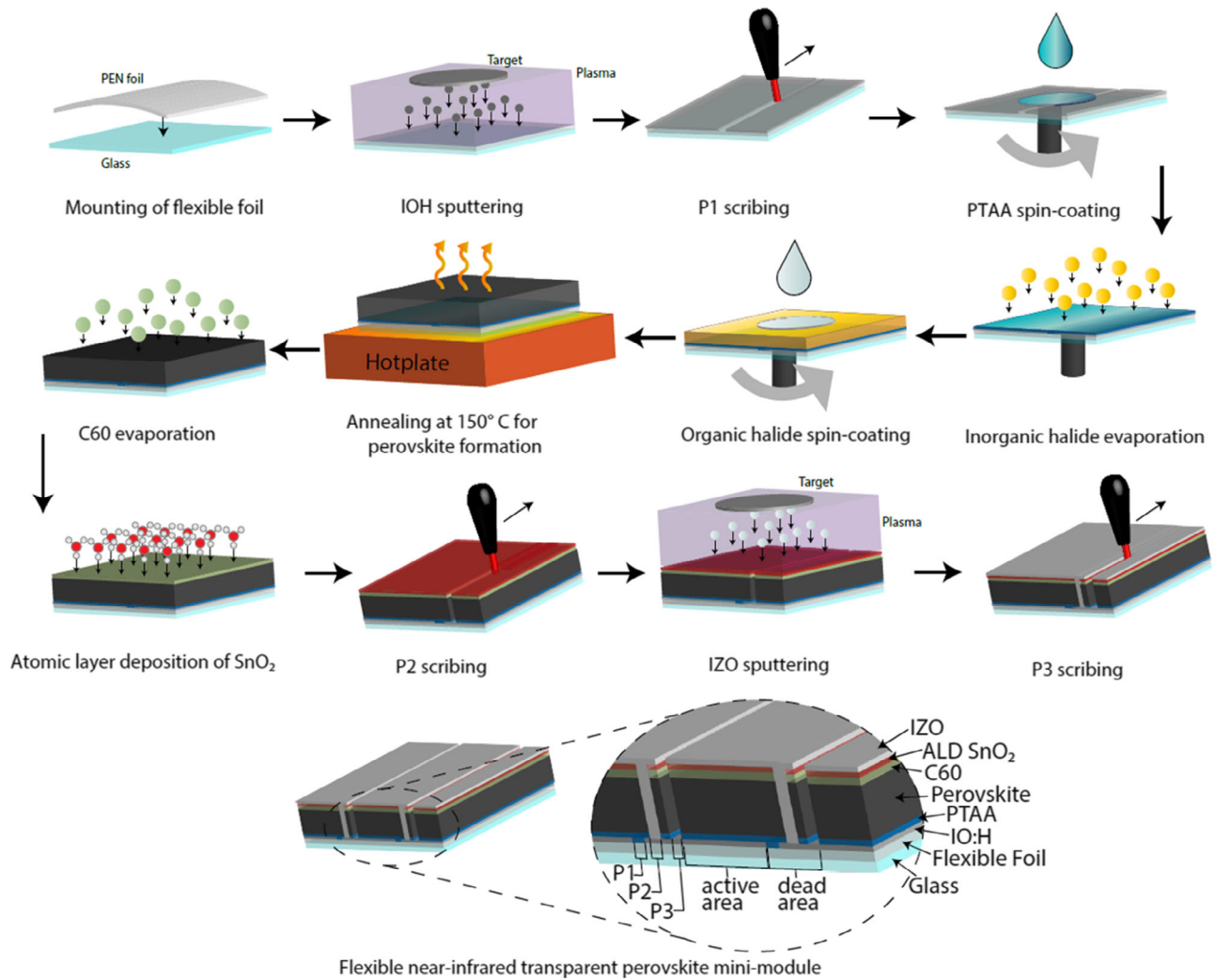


**Figure 1.** Processing sequence of flexible NIR-transparent perovskite mini-module. At the bottom, the monolithically interconnected flexible mini-module is shown with indication of the active and dead areas.

$$L_{\text{Front\_TCO}} = \frac{1}{3} R_{\text{sh\_Front}} \cdot \frac{J_{\text{MPP}}}{V_{\text{MPP}}} \cdot \frac{W_A^3}{(W_A + W_D)} \quad (1)$$

$$L_{\text{Rear\_TCO}} = \frac{1}{3} R_{\text{sh\_Rear}} \cdot \frac{J_{\text{MPP}}}{V_{\text{MPP}}} \times \frac{W_A^3}{(W_A + W_D)} \quad (2)$$

$$L_{\text{Dead area}} = \frac{W_D}{(W_A + W_D)} \quad (3)$$

$$L_{\text{Total}} = L_{\text{Front\_TCO}} + L_{\text{Rear\_TCO}} + L_{\text{Dead area}} \quad (4)$$

The contribution of resistive loss (by Equation (2) with  $J_{\text{MPP}} = 12.87 \text{ mA cm}^{-2}$ ,  $V_{\text{MPP}} = 0.85 \text{ V}$ ,  $W_D = 700 \mu\text{m}$ ) as a function of sheet resistance of the rear TCO is shown in **Figure 2a**. The fraction of resistive loss in a mini-module increases with  $W_A$ , and gets severe with the use of a highly resistive electrode. The magnitude of the current is rather low in small area cells ( $<0.1 \text{ cm}^2$ ); hence, the resistive electrodes have limited influence on device performance. However, as the magnitude of

the current scales up with the width of the active area in a mini-module, resistive electrodes impart substantial amount of ohmic power losses. In an earlier work on NIR-transparent perovskite mini-module,<sup>[25]</sup> TCOs with a sheet resistance of 25 and  $65 \Omega \text{ sq}^{-1}$  were utilized as the front and rear electrodes to enable NIR-transparency. To reduce resistive losses, they designed mini-modules with seven monolithically interconnected subcells with a narrow active area width of 2.86 mm. Due to a higher fraction of interconnection width, the GFF of the mini-modules was limited to 91%. In the present work, we utilize transparent electrodes with a sheet resistance of less than  $10 \Omega \text{ sq}^{-1}$  for the front (IO:H) and rear (IZO) electrodes to allow the use of wider subcells to improve the GFF of the mini-module. Further, the low free carrier absorption in these electrodes enables high conductivity but with low parasitic absorption losses. The use of low resistive TCO reduces the fraction of resistive loss (Figure 2a) to below 5%, even for an active area width of 12 mm.

For an optimal trade-off between the resistive and dead area losses, we evaluated the total relative power loss

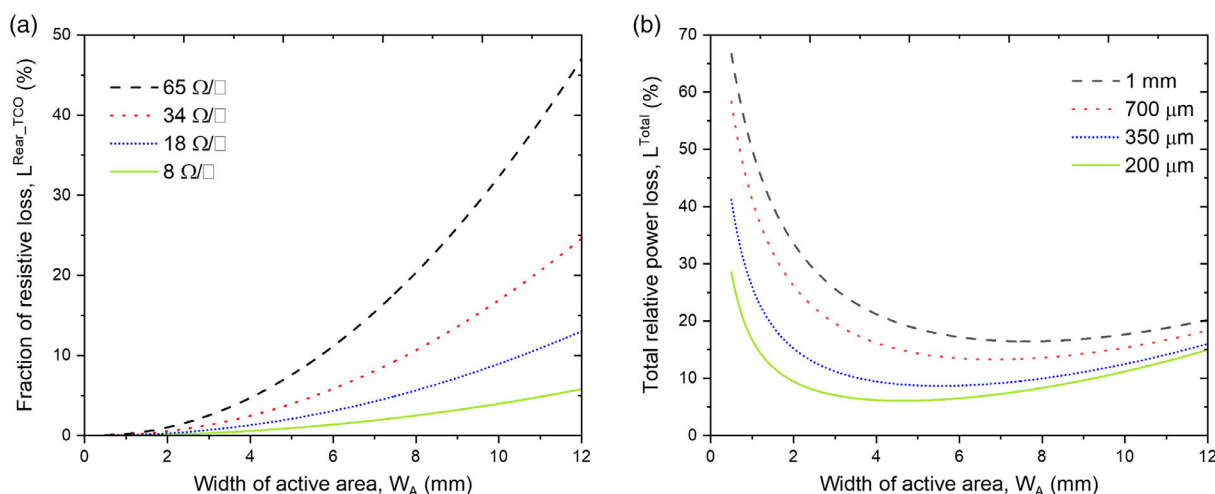


**Figure 2.** Analytical analysis for mini-module layout optimization. a) Fraction of resistive power loss due to rear TCO as a function of active-area width for rear TCO with different sheet resistance. b) Total relative power loss as a function of active area width for different interconnection widths.

(by Equation (4) with  $R_{\text{SH-Front}} = 9.7 \Omega \text{sq}^{-1}$ ,  $R_{\text{SH-Rear}} = 8 \Omega \text{sq}^{-1}$ ,  $J_{\text{MPP}} = 12.87 \text{ mA cm}^{-2}$ ,  $V_{\text{MPP}} = 0.85 \text{ V}$ ) in a mini-module against  $W_A$  for different interconnection widths. As shown in Figure 2b, a reduction in the interconnection width substantially reduces the total relative power loss, due to improved utilization of the aperture area, and a loss below 10% is possible for a wider  $W_A$  (4–6 mm) but with a narrow interconnection width of 200–350  $\mu\text{m}$ . The total relative power loss can further be reduced by narrowing the interconnection width.

## 2.2. Development of Laser Scribing for Interconnection in Flexible NIR-Transparent Perovskite mini-module

Monolithic interconnection (Figure 1) can be achieved using three patterning steps, namely, P1, P2, and P3 to split a large-area cell into subcells, and interconnect them in series. Briefly, the P1 scribing electrically isolates the front IO:H electrode into individual areas. P2 scribing is performed prior to the rear IZO electrode deposition to create a pathway to interconnect the front and rear electrodes. Finally, P3 scribing isolates the rear IZO electrode to form individual subcells and realize series interconnection.

All the patterning steps were carried out using a 1064 nm NIR-laser source with a fiducial-based alignment system for high precision scribing.<sup>[26,27]</sup> In general, P1 and P3 scribe with residual electrode will result in electrical shunts. Likewise, P2 scribe with improper removal of the functional layers or with any damage to the IO:H electrode can increase the series resistance in the mini-module.<sup>[22,28]</sup> These can negatively impact the mini-module performance. Considering these aspects, we optimize the laser scribing of NIR-transparent perovskite mini-module and evaluate them through optical and electrical analysis.

Compared to the rigid substrate, P1 patterning on a flexible substrate is challenging. In general, a wide laser processing window comprising of a laser pulse with maximum fluence and multiple repetitions can be applied to ablate any transparent electrode on a rigid substrate.<sup>[18,21]</sup> However, the absorption of

the laser pulse in the flexible foil induces thermal damage to the substrate at a higher laser pulse intensity. This narrows the laser processing window on a flexible substrate. Figure S3, Supporting Information, compares the confocal image of P1 scribe on rigid and flexible substrates using a high laser fluence ( $2.4 \text{ J cm}^{-2}$ ) with multiple repetitions (12). Although, in both the cases, the scribing process ablates the IO:H electrode and electrically isolates ( $>2 \text{ M}\Omega$ ) the adjacent regions from each other, the high laser pulse induces damage to the flexible substrate. The scribing damage in the flexible substrate creates a rough trench at the P1 scribe, which adversely affects further processing by disrupting the uniform flow of solution during the spin-coating process. We mitigate the physical damage to the flexible substrate by applying a laser fluence close to  $2 \text{ J cm}^{-2}$  (no repetitions) with a line and pulse overlap of over 50% to ablate the TCO electrode (Figure 3a) on the flexible substrate. The resistance of several  $\text{M}\Omega$  over the P1 scribe proves electrical isolation between adjacent areas.

It is essential to understand the ablation behavior of the IO:H electrode covered with HTL/Perovskite/ETL stack to identify the minimum laser fluence which can induce IO:H ablation. This is to accordingly ensure the limits of the laser processing window for P2 scribing. Figure S4, Supporting Information, shows the confocal image of a scribed region of a sample with a HTL/perovskite/ETL layer stack on an IO:H-coated PEN substrate with different laser fluences. At a laser fluence of  $0.88 \text{ J cm}^{-2}$ , removal of all the constituent layer is accomplished but with severe damage to the IO:H electrode and PEN substrate. With a decrease in the laser fluence ( $0.35 \text{ J cm}^{-2}$ ), a large traces of scribing residue (highlighted in Figure S4, Supporting Information) from incomplete removal of constituent layers are observed. At a laser fluence of  $0.5 \text{ J cm}^{-2}$ , P2 scribe (Figure 3b) with minimal residue and without inducing any damage to the IO:H electrode is accomplished. To electrically verify the P2 scribing, small squares were scribed out from flexible substrate with IO:H/PTAA/perovskite/ $\text{C}_{60}/\text{SnO}_2$  layer stack using different P2 scribing parameters. The sheet resistance of the P2 scribed regions



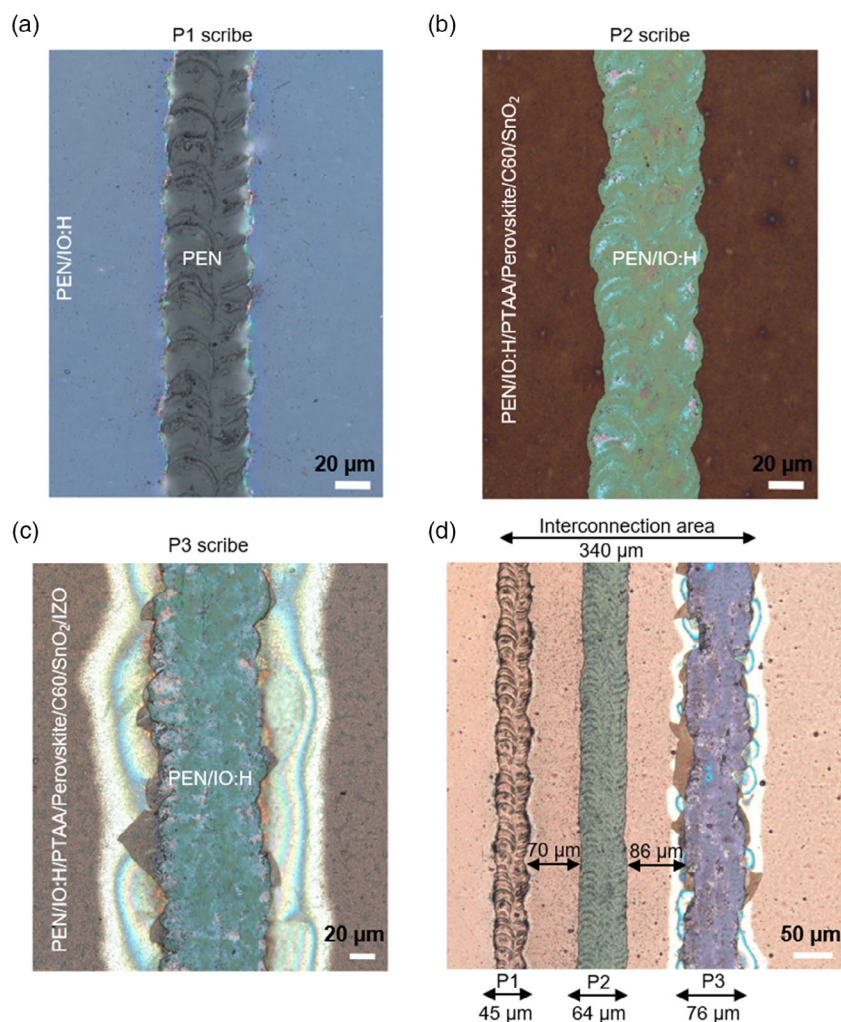


**Figure 3.** Optical evaluation of laser scribe on flexible PEN substrate. Confocal microscope image of a) P1, b) P2, and c) P3 scribe; and total width of d) interconnection.

was measured and compared with the bare IO:H electrode ( $10 \Omega \text{ sq}^{-1}$ ). For squares scribed with a fluence of  $0.5 \text{ J cm}^{-2}$ , a sheet resistance of around  $12 \Omega \text{ sq}^{-1}$  was achieved.

P3 scribing is carried out to isolate the rear IZO electrode from the two adjacent cells.<sup>[14,17,18]</sup> A non-uniform scribing line with residual IZO electrode will create electrical shunts. Mechanical scribing of transparent rear electrode for P3 patterning works on glass substrate<sup>[13,14]</sup> but not on the flexible substrates. In previous works, mechanical scribing was used to carry out the P3 interconnection for NIR-transparent mini-module. Further, the P3 scribing with laser has specific challenges. The electrode removal does not occur by laser-induced ablation but through a laser-induced lift-off process. The functional layers beneath the IZO electrode absorb the incident laser pulse, heat up, and the vaporized product ruptures the IZO electrode. The rupture of the brittle IZO results in cracks and delamination of the electrode in the neighboring regions (Figure S5, Supporting Information) of the P3 scribe. Scribing parameters similar to the P2 ( $0.5 \text{ J cm}^{-2}$ ) were used for P3 patterning. A pulse overlap of over 50% was maintained to ensure complete removal

of IZO electrode. The confocal microscope image (Figure 3c) after P3 scribing shows the clear removal of all the functional layers until the IO:H electrode and top isolation of neighboring cells. Similar to P1 scribing, the electrical isolation between the adjacent cells was verified by measuring high resistance over the P3 scribe. At the moment, delamination (Figure 3c) on the sides of the scribing line is apparent due to the brittle IZO electrode. In our future work, the P3 scribe will be optimized further either by the use of an alternative rear electrode or by using a different laser source for scribing.

As shown in Figure 3d, the width of P1, P2, and P3 is 45, 64, and 76  $\mu\text{m}$ , respectively, and safety margins between P1-P2 and P2-P3 scribes are provided to prevent overlap of the patterning regions. A relatively higher safety margin is provided between P2 and P3 to prevent any shunts originating from the blistered IZO electrode. Collectively, a total width of close to 340  $\mu\text{m}$  is used to realize monolithic interconnection. The scribing width obtained in this work can still be improved. The safety margin between P1-P2 and P2-P3 can further be reduced, and a narrower width of scribing lines is a work for future development.

### 2.3. Performance of NIR-Transparent Flexible Perovskite mini-module

Using the laser scribing conditions as described in the previous section, we demonstrate a proof-of-concept NIR-transparent perovskite mini-module on a flexible substrate with three monolithically interconnected subcells, each with an active area width of 4.6 mm. The interconnection width of 340  $\mu\text{m}$  is achieved which yields mini-modules with a GFF of over 93%. A cell to mini-module relative efficiency loss of less than 10% (Table S1, Supporting Information) is achieved through an optimized scribing and mini-module layout design. An antireflection coating (ARC) was applied on the front and rear side of the mini-module to minimize reflection losses. **Figure 4a** shows the  $J$ - $V$  characteristics of the mini-module illuminated from the IO:H front electrode. The corresponding PV parameters are tabulated in the plot. The mini-module performs at an efficiency close to 10.9% and delivers an MPP efficiency of 10.74% (Figure 4b). Further, the mini-module demonstrates an excellent bifaciality factor<sup>[29]</sup> ( $\eta_{\text{rear}}/\eta_{\text{front}}$ ) close to 95%. (Figure S6, Supporting Information)

As shown in Figure 4c, the mini-module has an average transmittance of over 75% in the NIR range, making it suitable for tandem application. However, it transmits photons in the visible region of the spectrum (below 700 nm), indicating incomplete absorption of high-energetic photons in the perovskite absorber. The light-harvesting potential of the NIR-transparent mini-module can be improved by utilizing a thicker wide-bandgap (WBG) perovskite absorber with excellent optoelectronic properties.

Electroluminescence (EL) (Figure 4d) and dark lock-in thermography (Figure S7, Supporting Information) measurements were carried out to characterize the homogeneity of the constituent layers and qualitatively access the monolithic interconnections in the mini-module. The EL image confirms that the mini-module has three monolithically interconnected subcells. The luminescence intensity in the mini-module shows an attenuated intensity in the peripheral regions of the subcells. Generally, the dynamic spin-coating is uniform on a small-area substrate and does not produce any streaky patterns.<sup>[15]</sup> However, in our case, the P1 scribe disrupts the uniform spread of the

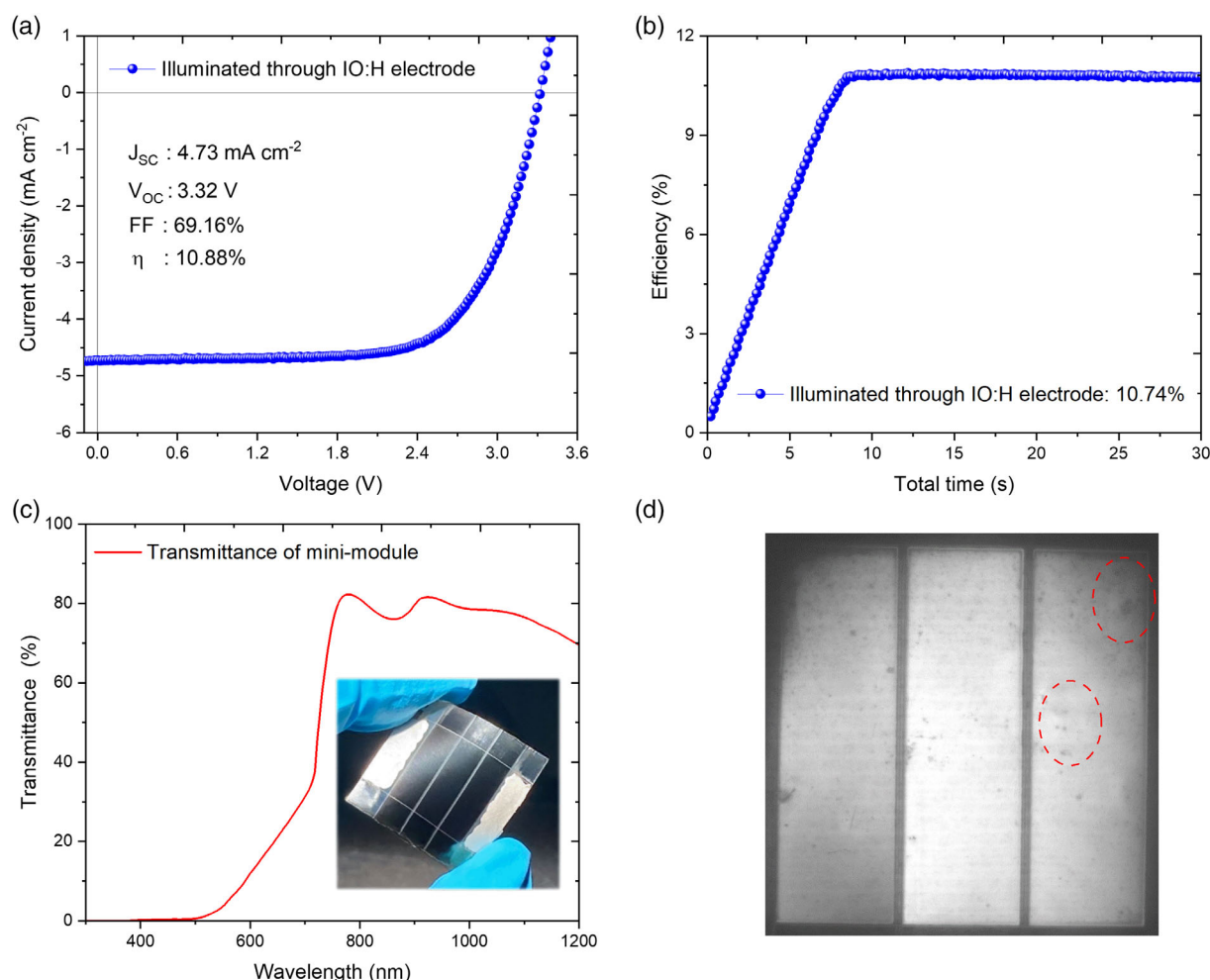


**Figure 4.** Evaluation of NIR-transparent perovskite mini-module. a) The current density–voltage ( $J$ - $V$ ) curve, b) steady-state efficiency, c) the transmittance curve with a photograph of mini-module, and d) EL image of the NIR-transparent perovskite mini-module. For (a) and (b), the mini-modules were illuminated through IO:H front electrode and measured at the MPP conditions. All the measurements were performed under simulated AM1.5 G irradiation conditions. The  $J$ - $V$  scans are carried out under backward scan conditions from  $V_{OC}$  to  $J_{SC}$ .

dispensed solvent during the spin-coating process, and compromises the uniformity of the layers. Apart from this inhomogeneity, a few dark spots (dotted circles) in the EL image are caused by dust particles originating from the processing samples in a non-clean room environment. The results of the EL indicate that spin coating on a patterned flexible substrate is not the ideal processing method to realize uniform layers. Insights on future directions are explained in Section 2.5.

#### 2.4. Proof-of-Concept Flexible Perovskite-CIGS 4T Tandem mini-module

So far, there is no report on 4T flexible perovskite-CIGS mini-modules in the literature. Here, we combine the flexible NIR-transparent perovskite mini-module with a flexible CIGS mini-module in a 4T tandem architecture, as depicted in

**Figure 5a.** A CIGS mini-module consisting of five monolithically interconnected subcells with a stand-alone efficiency of 15.1% is used as the bottom mini-module in this work. An ARC coating is added to the CIGS mini-module to reduce reflection losses. The perovskite mini-module ( $2.20 \text{ cm}^2$ ) is placed as a filter directly on the CIGS bottom mini-module ( $2.03 \text{ cm}^2$ ) for tandem measurement.

The  $J$ - $V$  and EQE characteristic curves of the perovskite and CIGS bottom mini-module in a 4T tandem configuration are displayed in Figure 5b,c. The performance of the stand-alone CIGS mini-module is also included in the plot for the sake of comparison. The corresponding PV parameters are tabulated in Table 1. Compared to the stand-alone CIGS mini-module, the  $J_{SC}$  and  $V_{OC}$  of the CIGS mini-module are reduced in the tandem configuration due to reduced light intensity. The transmittance of the perovskite mini-module (Figure 5c) attenuates the photons received by the bottom mini-module, and as a result,

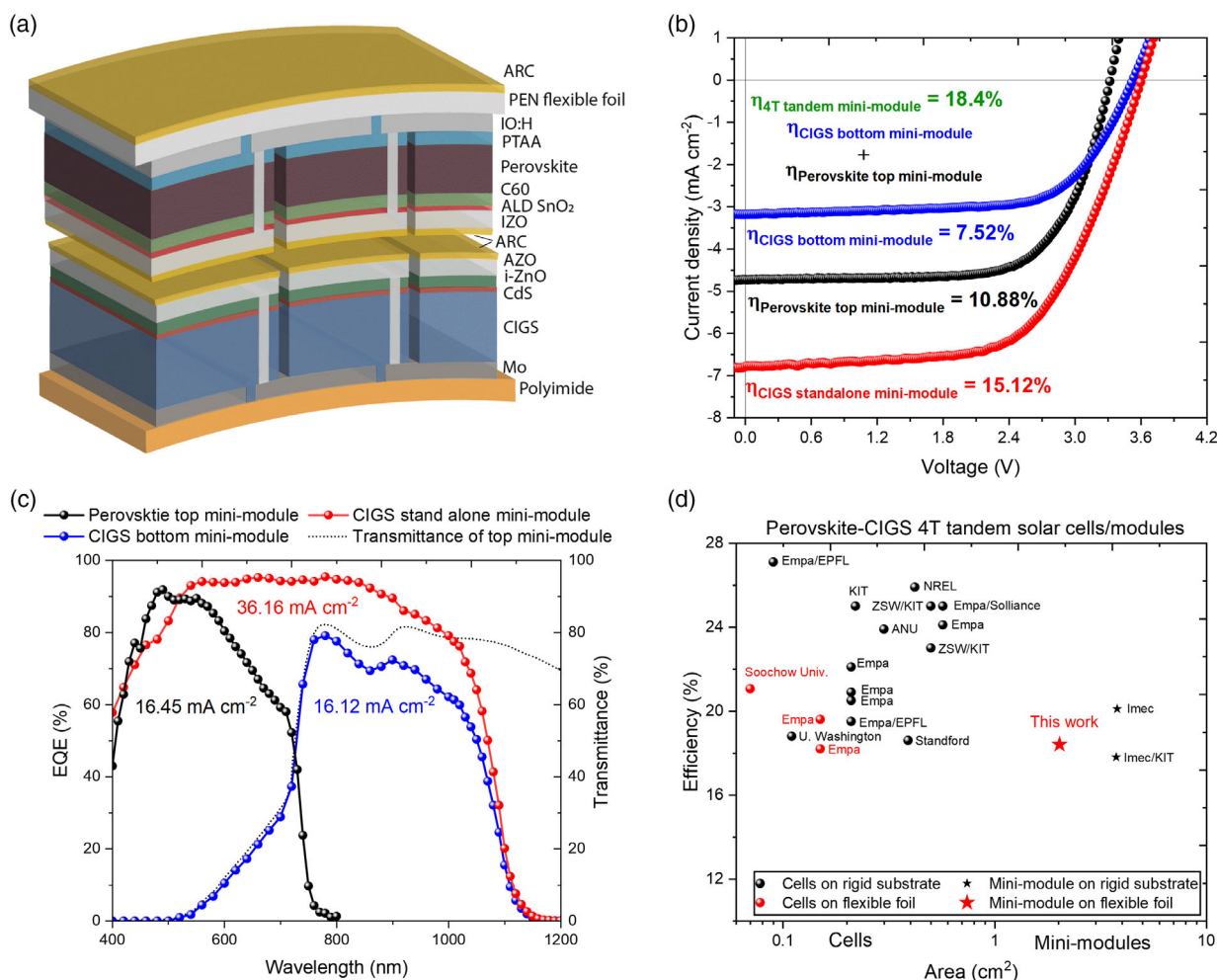


**Figure 5.** PV performance of flexible 4T perovskite-CIGS tandem mini-module. a) Schematic representation of flexible 4T tandem perovskite-CIGS mini-module. b) The  $J$ - $V$  and c) the external quantum efficiency EQE characteristics of NIR-transparent perovskite top mini-module (black), CIGS bottom mini-module (blue) in a 4T tandem configuration compared to the CIGS stand-alone mini-module (red). The transmittance of the perovskite top module is superimposed on the EQE curve of the bottom module to show the available photon flux for absorption. d) Reported efficiency of perovskite-CIGS tandem solar cells and mini-modules as a function of device area. To account for variation in top and bottom subcell areas, the subcell with the smallest aperture area is considered. The PV parameters corresponding to all the data points are tabulated in Table S2, Supporting Information.



**Table 1.** PV parameters of the flexible perovskite-CIGS tandem mini-module compared to the stand-alone CIGS mini-module.

Flexible mini-module	$V_{OC}$ [V]	$J_{SC}$ [mA cm <sup>-2</sup> ]	FF [%]	PCE [%]	Area [cm <sup>2</sup> ]
CIGS stand-alone mini-module	3.61	6.82	61.42	15.12	2.03
NIR-transparent perovskite mini-module	3.32	4.73	69.16	10.88	2.20
CIGS bottom mini-module	3.53	3.18	66.93	7.52	2.03
Tandem mini-module	–	–	–	18.4	–

an efficiency of 7.5% is obtained from the CIGS bottom mini-module. The flexible 4T perovskite-CIGS mini-module performs at an efficiency of 18.4% and outperforms both the perovskite and CIGS stand-alone mini-module. An absolute efficiency gain of 7.5% and 3.3% is achieved with respect to the perovskite and CIGS stand-alone mini-modules. Similarly, the steady-state efficiency of the 4T tandem mini-module (Figure S8, Supporting Information) is close to 18.2%, resulting in a substantial improvement in the device performance compared to the stand-alone single-junction mini-modules.

In an ideal scenario, the flexible top and bottom mini-module would be laminated together into a single component to realize flexible 4T tandem mini-module. At the moment, as a proof-of-concept demonstration, we show the potential of the NIR-transparent flexible perovskite mini-module in a 4T tandem configuration by stacking them on top of the CIGS mini-module as a filter to carry out tandem measurement. In our future demonstrations, as shown in Figure S1, Supporting Information, the flexible polymer sheet used for CIGS encapsulation would be used as a substrate for the NIR-transparent perovskite mini-module processing to directly integrate the flexible top and bottom mini-module in a 4T tandem configuration. An insulating sheet would be placed between the top and bottom mini-module as an optical coupler prior to lamination to prevent shunting issues.

Figure 5d shows the efficiency of perovskite-CIGS 4T tandem solar cells/mini-modules with their corresponding active area. Through our work, we tackle the challenges in realizing NIR-transparent perovskite mini-module on a flexible substrate and demonstrate a proof-of-concept flexible perovskite-CIGS 4T tandem mini-module, which serves as a starting point for further development. In the next section, we elaborate on the challenges and limitations of this work and focus on routes for further development.

## 2.5. Routes Toward Highly Efficient Flexible NIR-Transparent Perovskite Modules

Currently, the efficiency of the NIR-transparent perovskite mini-modules is mainly limited by the efficiency of the NIR-transparent perovskite solar cells. In the literature, opaque flexible solar cells with an efficiency over 19% have been realized using perovskite absorber with a bandgap of 1.68 eV.<sup>[30]</sup> However, in our case, the efficiency is close to 13%. This necessitates further improvement in efficiency at the cell level prior to efforts on upscaling. In our future studies, highly efficient WBG PSCs will be developed by improving the optoelectronic

properties of the perovskite absorber through compositional engineering and defect passivation strategies.<sup>[31–35]</sup> Further, the  $V_{OC}$  deficit in the WBG PSCs will be reduced by implementing different charge selective contacts and interfacial engineering.<sup>[36–40]</sup>

The perovskite absorber deposition for the flexible NIR-transparent perovskite mini-module is carried out using a combination of the thermal evaporation and spin coating method. However, for large-area demonstration, approaches to replace spin coating are essential. Further, to realize the vision of low-cost roll-to-roll processing, other functional layers which rely on vacuum-based deposition techniques need to make a transition to scalable solution-based methods.<sup>[41,42]</sup> Large-area uniform deposition of the perovskite and charge transport layer on the flexible substrate have already been achieved using solution-based scalable coating and printing techniques.<sup>[43]</sup> Fully R2R synthesized PSCs have shown rapid progress to achieve PCE of over 13%.<sup>[44]</sup>

The laser-based patterning developed in this work results in a significant dead area (7% of the aperture area) due to an interconnection width of 340  $\mu$ m. The GFF of the mini-module can be improved through reducing the safety margin between the scribing regions and by narrowing the scribing lines. At the moment, the safety margin between P1–P2 and P2–P3 accounts for almost 150  $\mu$ m width. Instead of a single-point fiducial alignment protocol, a multipoint alignment could be carried out to improve the precision of the scribing and reduce the safety margin. The P1 and P3 width reported in this work are 46 and 76  $\mu$ m, respectively. As the purpose of these scribes is to ensure isolation between the neighboring subcells, reducing their width would not have detrimental impact (provided the narrow scribes do not induce any shunting paths) on device performance. In the literature, P1<sup>[45,46]</sup> and P3<sup>[23,26,47]</sup> scribes with a width less than 30  $\mu$ m have been achieved for opaque perovskite mini-modules on rigid substrates. As a result of narrow interconnection region, these works show excellent GFF of over 95%. Efforts to achieve narrow scribing width equivalent to the state-of-the-art values would be scope for the future. Apart from the classical line interconnection scheme, point contact interconnection design can also be explored to achieve mini-module with excellent GFF.<sup>[48]</sup> Recently, Rakocevic and co-workers implemented the point contact interconnection design in rigid perovskite mini-module to achieve a GFF of 99%.<sup>[49]</sup>

The P2 interconnection connects the transparent conductive rear electrode with the front electrode of the adjacent cell to facilitate the monolithic interconnection of the subcells. To reduce the resistive losses at P2 interconnection, the sheet resistance of the top electrode needs to be as low as possible.<sup>[50]</sup> At the same time, the optical transparency of the rear electrode in the NIR region should not be compromised for the proper operation of the bottom cell. Under these considerations, we utilized transparent conductive electrode IZO as the rear electrode with a thickness of about 600 nm to facilitate a low resistive interconnection at the P2 trench. Although the transmittance of the top cell is about 75% in the region of interest, the parasitic losses due to absorption in the rear TCO cannot be overlooked. It is of extreme importance to develop transparent contact with superior conductivity and transparency for tandem application.<sup>[51]</sup>



### 3. Conclusion

To conclude, we demonstrated a proof-of-concept NIR-transparent flexible perovskite mini-module with an efficiency of 10.8% and a NIR-transparency of over 75%. An all-laser scribing interconnection was used to tackle the challenges related to monolithic interconnection on soft flexible PEN substrate. The total fraction of power loss in the module was minimized by using highly conductive front and rear TCOs, resulting in lower resistive losses and a wider subcell width, to achieve a GFF over 93%. The laser scribing interconnection and optimal mini-module layout design enabled us to achieve a cell to mini-module loss of less than 10%. Further, as a proof of concept, we demonstrated a flexible 4T perovskite-CIGS tandem mini-module with an efficiency of 18.4%. For our future work, we would focus on the development of high-efficiency WBG perovskite solar cells using solution-based scalable methods, and further reduce the interconnection width to achieve high-efficiency flexible NIR-transparent perovskite mini-module with a GFF beyond 96%.

### 4. Experimental Section

**Materials:** Flexible polyethylene naphthalate (PEN) substrate were purchased from Advanced Electron Technology Co., Ltd. The materials used for charge transport layer stack such as PTAA and Fullerene-C60 were purchased from Xi'an Polymer Light Technology Corp. The materials for inorganic halide evaporation such as  $\text{PbI}_2$  (>99%) and  $\text{CsI}$  (>99%), and for organic halide coating such as FAI (>99.99%) and FABr (>99.99%) were purchased from Tokyo Chemical Industry. All the aforementioned materials were weighed in a glove box filled with high-purity  $\text{N}_2$ . Copper ( $\text{Cu} \geq 99.99\%$ ) and toluene (anhydrous, 99.8%) were purchased from Sigma-Aldrich Pty Ltd. Anhydrous ethanol was purchased from VWR chemicals.

**Fabrication of Perovskite Mini-module:** Mini-module with a layer structure of PEN/IO:H/PTAA/perovskite/ $\text{C}_{60}$ /ALD  $\text{SnO}_2$ /IZO was adopted in this work. First, the PEN substrate was glued to the glass substrate with an epoxy resin. Then, hydrogenated indium oxide (IO:H) with a sheet resistance of  $10 \Omega \text{ sq}^{-1}$  was deposited on the flexible foil in a high-vacuum sputtering system (CT200, Alliance concept) by RF sputtering of ceramic  $\text{In}_2\text{O}_3$  targets (99.99%, 10 in. diameter, SPM AG) in a mixed  $\text{Ar}$ ,  $\text{O}_2$ , and  $\text{H}_2$  atmosphere at room temperature. P1 scribing to isolate the IO:H substrate to individual subcells was applied using an in-house laser scribing setup with a NIR-wavelength pulse laser source. A laser fluence of close to  $2 \text{ J cm}^{-2}$  was used to realize P1 scribing.

After the scribing process, the substrates were initially cleaned with ethanol to remove any scribing residues and were further cleaned by UV/Ozone treatment (Jelight Company Inc.) for 20 min. The cleaned substrates were transferred to an  $\text{N}_2$  filled glove box for further processing. The hole-transport PTAA layer was coated through dynamically spin coating a 35  $\mu\text{L}$  of PTAA solution (5  $\text{mg mL}^{-1}$  in toluene) at 6000 rpm (5 s acceleration) for 35 s, followed by thermal annealing at  $100^\circ\text{C}$  for 10 min. The PTAA-coated flexible substrates were transferred to an in-house developed thermal evaporator, where the inorganic halide templates were sequentially deposited. First, 12 nm of  $\text{CsI}$  ( $0.1 \text{ \AA s}^{-1}$ ) followed by a 235 nm of  $\text{PbI}_2$  ( $1.5 \text{ \AA s}^{-1}$ ) were deposited under vacuum conditions ( $< 6 \times 10^{-6}$  mbar). The samples were transferred again to the glove box to coat the organic halide solution. A 0.55 M of FAI:FABr solution with a volume ratio of 1:2 was utilized for preparing the organic halide solution. The organic halide template was dynamically spin-coated at 3000 rpm (5 s acceleration) for 35 s. The coated samples were annealed in a hot plate in ambient air at  $150^\circ\text{C}$  for 30 min to form perovskite layer. The substrates were then transferred into a vacuum chamber for thermal evaporation of  $\text{C}_{60}$  layer (20 nm,  $0.2 \text{ \AA s}^{-1}$ ) under a vacuum pressure at around

$4 \times 10^{-6}$  mbar. For buffer layer deposition, the samples were transferred to Fiji G2 ALD deposition system and the ALD process was performed at a substrate temperature of  $100^\circ\text{C}$  with argon as carrier gas at a base pressure of 0.4 mbar to deposit ALD  $\text{SnO}_2$  layer. Tetrakis(dimethylamino) tin(IV) (TDMASn) (Strem) and  $\text{H}_2\text{O}$  were used as the precursor, and TDMASn was kept at  $75^\circ\text{C}$  while  $\text{H}_2\text{O}$  was unheated. A 200 cycle of  $\text{SnO}_2$  was found to be optimum as a buffer layer for development of NIR-transparent mini-modules. The growth rate was determined by ellipsometry on Si (100) reference substrates and linear growth was observed with a growth rate of  $1.05 \text{ \AA}$  per cycle. The samples were subjected to P2 scribing with a laser fluence of  $0.5 \text{ J cm}^{-2}$  to remove all the functional layers without any damage to the front IO:H electrode. Finally, the samples were finished with an IZO rear electrode deposition by RF-magnetron sputtering followed by carrying out P3 scribing. The P3 scribing was carried out at  $0.5 \text{ J cm}^{-2}$  to ablate all the functional layers until the IO:H electrode. The P3 scribing was performed at a lower laser (factor of 3) speed compared to P2 scribing to realize a higher pulse overlap. The mini-module layout is displayed in Figure S9, Supporting Information, for additional information.

**Fabrication of CIGS Mini-module:**  $\text{Cu}(\text{In,Ga})\text{Se}_2$  (CIGS) absorber layer was deposited in a three-stage coevaporation growth process on a molybdenum (Mo)-coated flexible polyimide (PI) substrate, and underwent an alkali postdeposition treatment. More details on the fabrication process can be found elsewhere.<sup>[52]</sup> The stacking sequence of the completed solar cell is PI/Mo/CIGS/CdS/i-ZnO/ZnO:Al/ZnO:In.

The mini-modules were conducted on a  $5 \text{ cm} \times 5 \text{ cm}$  large PI substrate with three individual units. Each module interconnects six  $0.5 \text{ cm}^2$  cells. In the laser scribing process (P1 step), the Mo was patterned with an IR laser ( $1.23 \text{ J cm}^{-2}$ ). Second, the CIGS absorber, CdS, i-ZnO, and thin AZO layer were segmented (P2 step) by a quasicontinuous 1070 nm laser ( $1.9 \text{ W}$ ). Third, a highly conductive thick IZO was deposited and scribed again (P3 step) with an IR laser ( $0.46 \text{ J cm}^{-2}$ ). Finally, the Mo layers were removed by mechanical scribing to separate the individual units (PT step). The CIGS mini-module layout is provided in Figure S10, Supporting Information, for additional information.

**Device Characterization: J–V Measurement:** For the photocurrent–voltage (J–V) characteristics, the mini-modules were tested under standard AM1.5 G illumination and were measured using a Keithley 2400 source meter under four-contact mode. A certified monocrystalline silicon solar cell (RS-ID-5, Fraunhofer-ISE) was used to calibrate a class ABA solar simulator (LOT-QuantumDesign) to 1 sun AM1.5 G illumination. All the J–V measurements were carried out under backward scan conditions (from  $V_{\text{OC}}$  to  $J_{\text{SC}}$ ). The measurement stage was maintained at a steady-state temperature by a cooling system. For carrying out the steady-state efficiency measurement, a MPP tracking system with perturb and observe algorithm method was used to record the efficiency as a function of time.

**EQE Measurement:** The EQE of the mini-modules was measured using an in-house developed setup. The probing beam was generated by a chopped white source (900 W, halogen lamp, 280 Hz) and a dual grating monochromator. The beam size was adjusted to ensure an illumination area within the cell area. A monocrystalline silicon solar cell (RS-ID-5, Fraunhofer-ISE) was used as a reference cell. White bias light was applied during the measurement with an intensity of  $\approx 0.1$  sun.

**Fib SEM:** The microstructure of the perovskite device stack was studied by scanning electron microscopy (SEM) (Helios NanoLab 600 DualBeam). The cross section was prepared by means of a FEI Helios NanoLab 600 focused ion beam (FIB) operated at accelerating voltages of 30 and 5 kV. A thin layer of platinum coating on the top of the probed sample was coated to avoid any charging effects.

**UV–Vis Spectroscopy:** The total transmittance (T) and reflectance (R) spectra were acquired using an UV–vis–NIR spectrophotometer (Shimadzu UV-3600) equipped with an integrating sphere.

**Confocal Measurement:** Images were acquired with LEICA DCM8 with the bright field in default operation mode with  $5\times$ ,  $20\times$ , and  $50\times$  EPI-L objectives. Images were constructed using the smart area stitching correlation.

**EL:** The EL images were recorded by probing the perovskite mini-module in forward bias with 10 mA source current at a bias over open-circuit

voltage condition with an acquisition time of 400 ms. The luminescence was measured using a high-resolution digital B/W CCD camera ORCA-ER from Hamamatsu.

**Lock in Thermography:** The measurements were carried out with an infra-red camera system ImageIR 9400 from InfraTec using a stirring cooled InSb detector. The modules were probed in forward bias applying +3.3 V and a lock-in frequency of 1 Hz, while the detector frame rate was set at 200 Hz.

## Supporting Information

Supporting Information is available from the Wiley Online Library or from the author.

## Acknowledgements

This work was supported by funding from the Swiss Federal Office of Energy (SFOE)-BFE (project no.: SI/501805-01), Swiss National Science Foundation (SNF)-Bridge (project no.: 20B2-1\_176552/1), European Union's Horizon 2020 research and innovation program under grant agreement no. 850937, Swiss Federal Office of Energy (SFOE) (SI/502310-01 "ACIGS"), and the Swiss National Science Foundation (SNSF) under grant no. 200021\_197144/1 ("CIS"). The authors acknowledge the financial support from the Strategic Focus Area Advanced Manufacturing under the project AMYS—Advancing manufacturability of hybrid organic–inorganic semiconductors for large-area optoelectronics. H.L. thanks the funding of China Scholarship Council (CSC) from the Ministry of Education of P. R. China. C.M.W. thanks the European Commission for funding through Marie Skłodowska-Curie Actions (Grant No. 101033077) K.A. and C.M.W. thank the Swiss National Science Foundation (PAPET, 197006) and the Swiss Federal Office of Energy (PRESTO) for funding. The Laboratory for Transport at Nanoscale Interfaces at Empa is gratefully acknowledged for granting access to lock-in thermography and FIB SEM measurements.

Open access funding provided by ETH-Bereich Forschungsanstalten.

## Conflict of Interest

The authors declare no conflict of interest.

## Data Availability Statement

The data that support the findings of this study are available from the corresponding author upon reasonable request.

## Keywords

flexible tandems, laser patterning, perovskite mini-modules, perovskites

Received: May 2, 2022

Revised: May 20, 2022

Published online:

- [1] N. G. Park, *Mater. Today* **2015**, 18, 65.
- [2] H. S. Jung, N. G. Park, *Small* **2015**, 11, 10.
- [3] H. Min, D. Y. Lee, J. Kim, G. Kim, K. S. Lee, J. Kim, M. J. Paik, Y. K. Kim, K. S. Kim, M. G. Kim, T. J. Shin, S. Il Seok, *Nature* **2021**, 598, 444.
- [4] R. K. Kothandaraman, Y. Jiang, T. Feurer, A. N. Tiwari, F. Fu, *Small Methods* **2020**, 4, 1.
- [5] S. Pisoni, F. Fu, R. Widmer, R. Carron, T. Moser, O. Groening, A. N. Tiwari, S. Buecheler, *Nano Energy* **2018**, 49, 300.
- [6] S. A. Hashemi, S. Ramakrishna, A. G. Aberle, *Energy Environ. Sci.* **2020**, 13, 685.
- [7] S. Pisoni, F. Fu, T. Feurer, M. Makha, B. Bissig, S. Nishiwaki, A. N. Tiwari, S. Buecheler, *J. Mater. Chem. A* **2017**, 5, 13639.
- [8] K. L. Wang, Y. H. Zhou, Y. H. Lou, Z. K. Wang, *Chem. Sci.* **2021**, 12, 11936.
- [9] C. Zhang, M. Chen, F. Fu, H. Zhu, T. Feurer, W. Tian, C. Zhu, K. Zhou, S. Jin, S. M. Zakeeruddin, A. N. Tiwari, N. P. Padture, M. Grätzel, Y. Shi, *Energy Environ. Sci.* **2022**, 15, 1536.
- [10] M. Jošt, E. Köhnen, A. Al-Ashouri, T. Bertram, Š. Tomšič, A. Magomedov, E. Kasparavicius, T. Kodalle, B. Lipovšek, V. Getautis, R. Schlattmann, C. A. Kaufmann, S. Albrecht, M. Topič, *ACS Energy Lett.* **2022**, 7, 1298.
- [11] S. Li, C. Wang, D. Zhao, Y. An, Y. Zhao, X. Zhao, X. Li, *Nano Energy* **2020**, 78, 105378.
- [12] F. Fu, S. Nishiwaki, J. Werner, T. Feurer, S. Pisoni, Q. Jeangros, S. Buecheler, C. Ballif, A. N. Tiwari, **2019**, arXiv preprints arXiv:1907.10330v1.
- [13] M. Jaysankar, S. Paetel, M. Debucquoy, E. Ahlswede, R. Gehlhaar, J. Poortmans, in *IEEE 7th World Conf. Photovolt. Energy Conversion, WCPEC 2018 - A Jt. Conf. 45th IEEE PVSC, 28th PVSEC 34th EU PVSEC*, IEEE, Piscataway, NJ **2018**, pp. 3584–3587.
- [14] U. W. Paetzold, M. Jaysankar, R. Gehlhaar, E. Ahlswede, S. Paetel, W. Qiu, J. Bastos, L. Rakocevic, B. S. Richards, T. Aernouts, M. Powalla, J. Poortmans, *J. Mater. Chem. A* **2017**, 5, 9897.
- [15] N. G. Park, K. Zhu, *Nat. Rev. Mater.* **2020**, 5, 333.
- [16] J. Hüpkens, J. Müller, B. Rech, *Springer Ser. Mater. Sci.* **2008**, 104, 359.
- [17] L. Vesce, M. Stefanelli, F. Matteocci, L. A. Castriotta, E. Lamanna, J. Herterich, F. Di Giacomo, M. Kohlstadt, U. Wurfel, A. Di Carlo, in *12th AEIT Int. Annu. Conf. AEIT 2020* **2020**.
- [18] C. Baillie, C. Eberspacher, T. Gehan, R. Bramante, M. Van Hest, *Conf. Rec. IEEE Photovolt. Spec. Conf.* **2019**, 2, 3468.
- [19] Y. Jiang, T. Feurer, R. Carron, G. T. Sevilla, T. Moser, S. Pisoni, R. Erni, M. D. Rossell, M. Ochoa, R. Hertwig, A. N. Tiwari, F. Fu, *ACS Nano* **2020**, 14, 7502.
- [20] F. Fu, L. Kranz, S. Yoon, J. Löckinger, T. Jäger, J. Perrenoud, T. Feurer, C. Gretener, S. Buecheler, A. N. Tiwari, *Phys. Status Solidi Appl. Mater. Sci.* **2015**, 212, 2708.
- [21] S. J. Moon, J. H. Yum, L. Lofgren, A. Walter, L. Sansonnens, M. Benkhaira, S. Nicolay, J. Bailat, C. Ballif, *IEEE J. Photovolt.* **2015**, 5, 1087.
- [22] A. Walter, S. J. Moon, B. A. Kamino, L. Lofgren, D. Sacchetto, F. Matteocci, B. Taheri, J. Bailat, A. Di Carlo, C. Ballif, S. Nicolay, *IEEE J. Photovolt.* **2018**, 8, 151.
- [23] A. L. Palma, F. Matteocci, A. Agresti, S. Pescetelli, E. Calabrò, L. Vesce, S. Christiansen, M. Schmidt, A. Di Carlo, *IEEE J. Photovolt.* **2017**, 7, 1674.
- [24] B. Turan, S. Haas, *J. Laser Micro Nanoeng.* **2013**, 8, 234.
- [25] M. Jaysankar, W. Qiu, M. van Eerden, T. Aernouts, R. Gehlhaar, M. Debucquoy, U. W. Paetzold, J. Poortmans, *Adv. Energy Mater.* **2017**, 7, 1602807.
- [26] D. B. Ritzer, T. Abzieher, A. Basibüyük, T. Feeney, F. Laufer, S. Ternes, B. S. Richards, S. Bergfeld, U. W. Paetzold, *Prog. Photovolt. Res. Appl.* **2022**, 30, 360.
- [27] E. Lohmüller, J. Weber, M. Demant, S. Lohmüller, S. Gutscher, P. Saint-Cast, A. Wolf, *Prog. Photovolt. Res. Appl.* **2020**, 28, 189.
- [28] Z. Yang, Z. Liu, V. Ahmadi, W. Chen, Y. Qi, *Sol. RRL* **2022**, 6.
- [29] G. J. M. Janssen, K. C. J. Tool, E. J. Kossen, B. B. Van Aken, A. J. Carr, I. G. Romijn, *Energy Procedia* **2017**, 124, 76.
- [30] O. Almora, D. Baran, G. C. Bazan, C. Berger, C. I. Cabrera, K. R. Catchpole, S. Erten-Ela, F. Guo, J. Hauch, A. W. Y. Ho-

- Baillie, T. J. Jacobsson, R. A. J. Janssen, T. Kirchartz, N. Kopidakis, Y. Li, M. A. Loi, R. R. Lunt, X. Mathew, M. D. McGehee, J. Min, D. B. Mitzi, M. K. Nazeeruddin, J. Nelson, A. F. Nogueira, U. W. Paetzold, N. G. Park, B. P. Rand, U. Rau, H. J. Snaith, E. Unger, et al., *Adv. Energy Mater.* **2021**, *11*, 2002774.
- [31] X. Zheng, B. Chen, J. Dai, Y. Fang, Y. Bai, Y. Lin, H. Wei, X. C. Zeng, J. Huang, *Nat. Energy* **2017**, *2*, 1.
- [32] B. Chen, P. N. Rudd, S. Yang, Y. Yuan, J. Huang, *Chem. Soc. Rev.* **2019**, *48*, 3842.
- [33] J. Peng, J. I. Khan, W. Liu, E. Ugur, T. Duong, Y. Wu, H. Shen, K. Wang, H. Dang, E. Aydin, X. Yang, Y. Wan, K. J. Weber, K. R. Catchpole, F. Laquai, S. De Wolf, T. P. White, *Adv. Energy Mater.* **2018**, *8*, 1.
- [34] M. Abdi-Jalebi, Z. Andaji-Garmaroudi, S. Cacovich, C. Stavrakas, B. Philippe, J. M. Richter, M. Alsari, E. P. Booker, E. M. Hutter, A. J. Pearson, S. Lilliu, T. J. Savenije, H. Rensmo, G. Divitini, C. Ducati, R. H. Friend, S. D. Stranks, *Nature* **2018**, *555*, 497.
- [35] Q. Jiang, Y. Zhao, X. Zhang, X. Yang, Y. Chen, Z. Chu, Q. Ye, X. Li, Z. Yin, J. You, *Nat. Photonics* **2019**, *13*, 460.
- [36] A. Al-Ashouri, A. Magomedov, M. Roß, M. Jošt, M. Talaikis, G. Chistiakova, T. Bertram, J. A. Márquez, E. Köhnen, E. Kasparavičius, S. Levcenko, L. Gil-Escrig, C. J. Hages, R. Schlatmann, B. Rech, T. Malinauskas, T. Unold, C. A. Kaufmann, L. Korte, G. Niaura, V. Getautis, S. Albrecht, *Energy Environ. Sci.* **2019**, *12*, 3356.
- [37] M. Stolterfoht, P. Caprioglio, C. M. Wolff, J. A. Márquez, J. Nordmann, S. Zhang, D. Rothhardt, U. Hörmann, Y. Amir, A. Redinger, L. Kegelmann, F. Zu, S. Albrecht, N. Koch, T. Kirchartz, M. Saliba, T. Unold, D. Neher, *Energy Environ. Sci.* **2019**, *12*, 2778.
- [38] C. M. Wolff, F. Zu, A. Paulke, L. P. Toro, N. Koch, D. Neher, *Adv. Mater.* **2017**, *29*, 1.
- [39] J. P. Correa-Baena, W. Tress, K. Domanski, E. H. Anaraki, S. H. Turren-Cruz, B. Roose, P. P. Boix, M. Grätzel, M. Saliba, A. Abate, A. Hagfeldt, *Energy Environ. Sci.* **2017**, *10*, 1207.
- [40] M. Stolterfoht, C. M. Wolff, Y. Amir, A. Paulke, L. Perdígón-Toro, P. Caprioglio, D. Neher, *Energy Environ. Sci.* **2017**, *10*, 1530.
- [41] J. F. Benitez-Rodriguez, D. Chen, M. Gao, R. A. Caruso, *Sol. RRL* **2021**, *5*, 1.
- [42] T. Yang, Y. Y. Kim, J. Seo, *APL Mater.* **2021**, *9*, 110901.
- [43] T. Y. Yang, Y. Y. Kim, J. Seo, *APL Mater.* **2021**, *9*, 110901.
- [44] H. Li, C. Zuo, D. Angmo, H. Weerasinghe, M. Gao, J. Yang, *Nano-Micro Lett.* **2022**, *14*, 79.
- [45] F. Di Giacomo, L. A. Castriotta, F. U. Kosasih, D. Di Girolamo, C. Ducati, A. Di Carlo, *Micromachines* **2020**, *11*, 1.
- [46] M. Jeong, I. W. Choi, K. Yim, S. Jeong, M. Kim, S. J. Choi, Y. Cho, J. H. An, H. B. Kim, Y. Jo, S. H. Kang, J. H. Bae, C. W. Lee, D. S. Kim, C. Yang, *Nat. Photonics* **2022**, *16*, 119.
- [47] C. Wang, G. Tan, X. Luo, J. Li, X. Gao, Y. Mo, X. L. Zhang, X. Wang, F. Huang, *J. Power Sources* **2020**, *466*, 228321.
- [48] S. Haas, S. Krumscheid, A. Bauer, A. Lambert, U. Rau, *Prog. Photovoltaics Res. Appl.* **2013**, *21*, 972.
- [49] L. Rakocevic, G. Schöpe, B. Turan, J. Genoe, T. Aernouts, S. Haas, R. Gehlhaar, J. Poortmans, *Prog. Photovoltaics Res. Appl.* **2020**, *28*, 1120.
- [50] J. Li, H. Wang, X. Y. Chin, H. A. Dewi, K. Vergeer, T. W. Goh, J. W. M. Lim, J. H. Lew, K. P. Loh, C. Soci, T. C. Sum, H. J. Bolink, N. Mathews, S. Mhaisalkar, A. Bruno, *Joule* **2020**, *1*.
- [51] D. Zhang, M. Najafi, V. Zardetto, M. Dorenkamper, W. Verhees, X. Zhou, A. Senes, A. Gutjahr, I. Romijn, S. Veenstra, B. Geerligs, M. Creatore, T. Aernouts, R. Andriessen, in *2018 IEEE 7th World Conf. Photovolt. Energy Conversion, WCPEC 2018 - A Jt. Conf. 45th IEEE PVSC, 28th PVSEC 34th EU PVSEC*, IEEE, Piscataway, NJ **2018**, pp. 3575–3577.
- [52] R. Carron, S. Nishiwaki, T. Feurer, R. Hertwig, E. Avancini, J. Löckinger, S. Yang, S. Buecheler, A. N. Tiwari, *Adv. Energy Mater.* **2019**, *9*, 1900408.